

Coarse-grained hybrid simulation of liposomes

G. J. A. Sevink,* M. Charlaganov and J. G. E. M. Fraaije

Cite this: *Soft Matter*, 2013, 9, 2816

We developed a new hybrid model for efficient modeling of complete vesicles with molecular detail. Combining elements of Brownian dynamics (BD) and dynamic density functional theory (DDFT), we reduce the computational load of an existing coarse grained particle-based dissipative particle dynamics (DPD) model by representing the solvent as a continuum variable or a field, in a consistent manner. Both particle and field representations are spatially unrestricted and there is no need to treat boundaries explicitly. We focus on developing a general framework for deriving the parameters in this hybrid approach from existing DPD representations, and validate this new method *via* a comparison to DPD results. In addition, we consider a few proof of principle calculations for large systems, including a vesicle of realistic dimensions (~45 nm radius) containing ϕ (10^4) lipids simulated for ϕ (10^6) time steps, to illustrate the performance of the new method.

Received 29th October 2012
Accepted 18th December 2012

DOI: 10.1039/c2sm27492b

www.rsc.org/softmatter

Introduction

Although membrane remodeling represents an important functional mechanism in cells and liposomes, the detailed principal mechanisms and the fundamentals of the accompanying molecular rearrangements remain largely unknown. Computational approaches could potentially clarify the essence or 'ousia' in these systems, but there is a distinct trade-off between (chemical) resolution and the length of a feasible simulation pathway. In particular, the time resolution required for stable numerical integration of transport equations is dictated by the time scale of the fastest degree of freedom in the simulation model. While phenomena in experimental membrane remodeling take place in seconds or even longer, approaches at the finest relevant level – atomistic molecular dynamics (MD) – require a resolution in the order of femto-seconds. It is easy to see that this scale gap, spanning many orders of magnitude, renders atomistic simulation of these larger-scale collective phenomena computationally intractable.

Consequently, the focus in recent years has been on the development of coarse-grained approaches that reduce this gap, by averaging over fast, and often not decisive, degrees of freedom, while conserving the essentials at these larger scales. The latter, the issue of representability, *i.e.* whether the equivalent model is a 'good' representation of the original (finer-grained) model in terms of the underlying energy landscape, is a major challenge and plays a role at almost all levels of description, including atomistic models,¹ although explicit statements about the latter are seldom made.

Our starting point is a coarse-grained method that was developed with these issues in mind, and that has provided

substantial insight in several aspects of membrane dynamics. We show how the molecular detail in this method could be consistently linked to an even coarser continuum (field) model, to arrive at a new hybrid approach. Combining the efficiency of a field description (for the abundant solvent) with an explicit particle model (for the lipids in the membrane) has serious advantages, as it overcomes the restrictions of the individual methods. First, we shortly discuss particular issues in coarse-grained membrane modeling. We refer to a number of reviews^{2–4} for a broader overview of lipid membrane modeling efforts.

Two types of models are most frequently used for modeling lipid membranes at a coarse-grained level, and are equivalent in the incorporation of intramolecular forces, which are represented by bond, angle and torsion potentials with parameters derived from more detailed simulations. Coarse-grained molecular dynamics (CGMD) lumps atoms into supra-atomic 'beads' or chemical fragments, with non-bonded interactions that are defined as Lennard-Jones type of potentials. The CGMD parameters for these chemical fragments are obtained *via* an optimization procedure, using atomistic simulations and/or experiments to match, for instance, mutual bead solubilities.⁵ Although chemical specificity is sufficiently retained, and CGMD simulations were shown to provide proper quantitative agreement with experimental observables, the computational requirements remain severe due to the 'hard' LJ potentials, that dictate a relatively small time increment in Newton's equation of motion. Dissipative particle dynamics (DPD), combining aspects of MD and lattice-gas automata, acknowledges the notion that centers of mass of beads can overlap, and uses a soft potential for non-bonded interactions instead. Since the repulsive forces are much softer, the time step can be further increased and beads can easily escape the cage formed of their surrounding, accelerating the kinetics and bringing realistic

Leiden Institute of Chemistry, Leiden University, P.O. Box 9502, 2300 RA Leiden, The Netherlands. E-mail: a.sevink@chem.leidenuniv.nl

experimental time- and length-scales, of collective phenomena on a system level, within reach. However, as the number of atoms per bead is roughly equal in CGMD and DPD, the number of tracked positions is comparable and remains substantial. Several groups have contributed to the development of CGMD force-fields for lipids and more complicated molecules (see, for instance, ref. 5 and 6). A rigorous approach in this context, multiscale coarse-graining (MS-CG), that matches the forces in atomistic MD to those in coarse-grained MD *via* a variational principle, was recently used to bias a Gay–Berne (GB) ellipsoid liquid-crystal model and access the time and length scale associated with realistic liposomes.⁷ However, the use of the GB model is primarily discussed in terms of enhancing the configurational sampling required for force matching. An overview of the DPD modeling efforts in this area can be found in ref. 8 and 9. An early comparison of both CGMD and DPD to atomistic MD simulations was carried out by the group of Smit,¹⁰ and showed that DPD is a powerful method for realistic lipid modeling, but that the parameterization should be handled with care.

Here, we select DPD as a starting point for our hybrid method, and focus on the representation of Shillcock and Lipowsky,¹¹ where each bead represents a small number (4–5) of solvent molecules or a lipid fragment. It should be noted that this choice is not essential here, since our aim is to constitute a functional relationship between DPD and hybrid model parameters. The simulation results of Shillcock *et al.* were shown to reproduce several experimental macroscopic membrane properties, including thickness, lateral fluidity and stiffness, reasonably well. The non-uniqueness of this representation, on the other hand, is illustrated by the fact that the DPD model was later re-parameterized, due to the unrealistic lipid exchange rates between adhering bilayers, stemming from an almost vanishing energy barrier for lipid exchange, for the original parameter set.

The considerations that prompted the development of our hybrid approach are related to the arguments for introducing implicit solvent, so we shortly review. When modeling a small vesicle, of radius R , a simulation volume of size $L \sim R$ is needed to avoid strong boundary effects. As the part of the volume occupied by the sheet-like membrane scales like the area (R^2), the fraction of the membrane component decreases with increasing radius R like $R^2/L^3 \sim 1/R$. The efficiency of coordinate-based methodology can thus be significantly enhanced by sacrificing the solvent, which forces membrane formation through hydrophobic interactions locally and, on a larger scale, transports momentum and thus affects the dynamics of the system. Although the latter role of solvent is unlikely to be incorporated in any effective model, replacing the degrees of freedom associated with the solvent by *implicit* solvent is a popular route. The formidable theoretical effort of systematically averaging over solvent degrees of freedom is often replaced by the simpler but computationally challenging task of identifying phenomenological potentials that replace the explicit solvent–lipid interactions. The resulting solvent-free approaches were applied for the study of several membrane phenomena, with considerable success.^{4,12} It seems advantageous to also replace solvent beads in DPD by a more efficient

description, moreover, a description that circumvents the tedious parameterization procedures associated with a new methodology by exploiting existing and validated representations.

Our goal in this paper is to introduce such a method, that is efficient both in terms of memory and computational requirements, and serves as a starting point for further balancing (molecular) resolution and efficiency. The model presented here allows for a continuum (field) and coordinate-based (soft-core beads) representations in a *single* simulation volume, where the premise is that we couple the bead and field representations in a thermodynamically consistent fashion. If this condition is satisfied, the solvent *beads* can be freely replaced by a solvent concentration *field*, and, owing to the fact that the field–bead interactions are local, the total computational effort is significantly reduced. Fig. 1 illustrates this concept, for lipid DPD parameters of Shillcock and Lipowsky and the mapped new hybrid coupling parameters for lipid–solvent interactions. Although we focus on the fundamentals, we perform a proof of principle. Using a pre-assembled sheet, we analyze the membrane properties in the hybrid and the DPD model, and demonstrate that the hybrid model reproduces important DPD membrane properties such as structure and thickness. We show that lipids dispersed in solvent indeed self-assemble into larger domains in the hybrid model. To illustrate efficiency, we show that the hybrid model can simulate closing up of a large punctured vesicle.

An important observation is that this model serves as a stepping stone for further developments of more accurate and efficient membrane modeling tools. For instance, the current diffusive dynamic models (Brownian dynamics for the beads and Langevin model for the fields) can in principle be replaced by a hydrodynamic description, *i.e.* the standard DPD kinetic equation for the beads and a Navier–Stokes solver for the continuous (field) component. Moreover, replacing solvent beads by a field can be seen as a first and necessary step towards the rigorous development of a DPD model with implicit solvent. Such extensions will be the subject of future work.

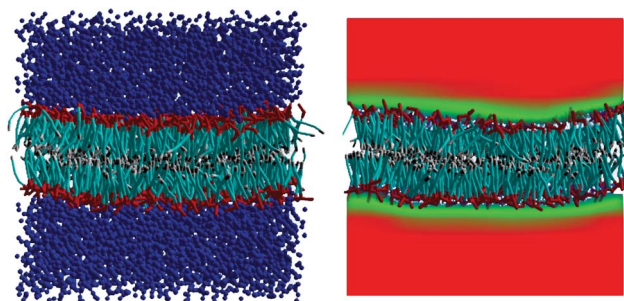


Fig. 1 Three dimensional simulation snapshots of dissipative particle dynamics (left) and the new hybrid method (right), illustrating the concept of replacing all solvent beads by a single solvent field. Field coloring is in agreement with solvent concentration values, and the field was made transparent below a threshold concentration. Particles are colored by their nature: head (red), tail (blue) and tail terminus (grey). The molecular detail and specific interactions of lipids are conserved in the hybrid method. The lipid concentration is equal in both cases and was selected in agreement with vanishing membrane tension.

General theory

From a conceptual viewpoint, the hybrid method allows for different representations of constituents, either coordinate-based (beads) or continuous (bead concentration fields), in a single simulation volume. To clearly distinguish between the two, we refer to coordinate-based beads as *particles* in the remainder. The heterogeneity of representation distinguishes this method from multi-scale approaches that aim at combining atomistic and mesoscopic representations in a hierarchical, sequential manner (mapping results from one level to another)¹³ of using the quasi-instantaneous field generated by the coordinate-based system for the efficient calculation of intermolecular interactions.^{14,15} We note, however, that such a hierarchical procedure is certainly not excluded in the current approach, and that this procedure potentially benefits from the particle–field mapping that is developed and validated in this hybrid method.

The hybrid free energy

We define a mesoscopic hybrid energy functional of the form

$$F = E^p + F^f + F^{pf} \quad (1)$$

where E^p and F^f are the potential energy and the free energy of the particle and field subsystem, respectively, and F^{pf} is a ‘coupling’ term that accounts for bringing the particles and fields together in one simulation volume. One should realize that this expression is very straightforward and generic, and only states that the hybrid functional reduces to the unperturbed field- or particle-based functionals for pure systems. The peculiarity is in the choice of two models with a similar coarsened molecular representations, and the requirement that a representation in either discrete or continuum variables is analogous. For the particles, we follow the conventions of dissipative particle dynamics (DPD) for soft-core particles. The potential energy E_p for monomeric fluids is explicitly given in terms of coordinates by

$$E_p = \sum_k \sum_{\forall l: r_{kl} < r_c} \frac{a_{kl}}{2r_c} (r_{kl} - r_c)^2 \quad (2)$$

where $r_{kl} = \|\mathbf{r}_k - \mathbf{r}_l\|_2$ is the distance between particles l and k and r_c is the cut-off distance that is, in accordance with standard practice, used as the unit of length. The pairwise interaction potential is characterized by the interaction strength a_{kl} , which only varies between different particle types. Bond, angle and/or torsion potentials of various kinds can be added to account for internal molecular properties and they contribute to E_p . For the continuous fields, *i.e.* concentrations for different types of particles $\rho_l(\mathbf{r})$, we select the free energy¹⁶

$$F^f[\rho_l] = F^{\text{id}}[\rho_l] + F^{\text{coh}}[\rho_l] + F^{\text{comp}}[\rho_l] \quad (3)$$

of the dynamic density functional theory (DDFT) (see, for details, van Vlimmeren *et al.*¹⁶), which is very similar to the free energy in the well-known self-consistent field (SCF) theory. The molecular representation is that of a fully flexible chain of

particles with Gaussian chain statistics, and the free energy in terms of $\rho_l(\mathbf{r})$ is obtained using the assumption that chains are always in *local* equilibrium. Besides an ideal F^{id} and pressure or compressibility F^{comp} terms, the free energy contains a mean-field interaction term F^{coh} that relates to standard Flory–Huggins theory. We can now specify the hybrid energy eqn (1) as

$$F[\{\mathbf{r}_k\}, \{\rho_l\}] = E^p(\{\mathbf{r}_k\}) + F^f[\{\rho_l\}] + F^{pf}(\{\mathbf{r}_k\}, \{\rho_l\}) \quad (4)$$

with E^p and F^f the standard potential energy for soft-core DPD-like particles and the DDFT free energy, respectively. A reasonable choice for the particle–field coupling interaction free energy is

$$F^{pf}(\{\mathbf{r}_k\}, \{\rho_l\}) = \int_V d\mathbf{r} \sum_{lk} c_{lk} \rho_l(\mathbf{r}) K(\mathbf{r} - \mathbf{r}_k), \quad (5)$$

where a normalized Gaussian smoothing kernel

$$K(\mathbf{r}) = \left(\frac{1}{\sigma^2 \pi}\right)^{3/2} \exp(-r^2/\sigma^2) \quad (6)$$

is used to map particles coordinate \mathbf{r}_k into fields (see Appendix A for discussion of the spread σ). The set of scalar coupling parameters c_{lk} defines the strength of interaction between the field of type l and the particle k . In the remainder, we use dimensionless units, unless mentioned otherwise. Energies are discussed in units $k_B T$, with T the temperature and k_B the Boltzmann constant, and, as mentioned, the cut-off distance r_c of the particle model is used as a unit of length.

There is a clear distinction in the way cohesive interactions and excluded volume are incorporated into DDFT and DPD. In the continuum DDFT model, these effects are separated into two different contributions to the free energies, F^{coh} and F^{comp} , and governed by the mean-field interaction parameters χ_{IJ} and Helfand compressibility parameter κ_H .¹⁶ In the particle description, the parameter a_{ij} in the pairwise interaction potentials plays a dual role, and for this reason it is commonly written as $a_{ij} = a_{ii} + \Delta a_{ij}$, where a_{ii} relates to the excluded volume and Δa_{ij} to cohesive interactions. Usually, $a_{ii} = a_0$ is assumed to be independent of the particle-type. Its proper value was previously determined¹⁷ from simulations for a monomeric DPD liquid by fitting pressures calculated using the virial theorem to a quadratic equation of state

$$p_p = \rho_p + \alpha a_0 \rho_p^2, \quad (7)$$

with ρ_p the particle density or number of particles per unit cell and $\alpha = 0.101 \pm 0.001$ a fitting parameter. Subsequently, the inverse isothermal compressibility is set to $\kappa^{-1} = 1 + 2\alpha a_0 \rho_p = 16$, the value for water at room temperature, providing $a_0 = 75/\rho_p$.¹⁷ Since the used α is the asymptotic value for $\rho_p \rightarrow \infty$, the procedure is only valid in a restricted ρ_p -range. In their seminal paper, Groot and Warren¹⁷ mention $\rho_p > 2$. For $\rho_p = 3$, the density that is also considered in the DPD simulations of Shillcock and Lipowsky,¹¹ one obtains the value $a_0 = a_{ii} = 25$.

Incorporating excluded volume or pressure coupling through a penalty function for (small) density fluctuations, which are assumed to be local and harmonic, was introduced

and discussed by Helfand.¹⁸ In practice, a proper value for κ_{H} in DDFT is determined by a rule of thumb, *i.e.* κ_{H} should be ‘large enough’ to allow only for small concentration fluctuations (or, alternatively, ensure an almost constant pressure), and ‘small enough’ to not completely damp any fluctuation. These rather loose conditions are usually monitored *via* F^{comp} during a calculation. We note that replacing the incompressibility condition $\sum_I \mu_I = 0$, with I the field index, by slight compressibility in DDFT is not compulsory,^{19,20} but that the numerical efficiency benefits substantially from resolving (part of) the stiffness of the set of dynamic equations that stems from the incompressibility condition.

In the hybrid model, however, the compressibility term in the free energy plays a very significant role and κ_{H} should be carefully chosen. We illustrate this by a simple example and assume a system containing particles and a single (solvent) field. The particles will affect the field by creating (field) cavities through the coupling interactions. Since the DDFT part of the hybrid free energy only considers the solvent field, the chemical potential due to the compressibility term, μ^{comp} , generates a solvent flux towards this cavity, the magnitude of which scales with κ_{H} . In equilibrium, $\mu^{\text{comp}}(\kappa_{\text{H}}, \rho_{\text{S}})$ and the coupling chemical potential μ^{cp} are balanced. The value of κ_{H} , a global variable, could be derived based on desired global features of the hybrid system, but such an exercise is complicated by the calculation of the pressure, either *via* the virial route^{17,21} or *via* compressibility, that requires simulation to access the ensemble-averaged contribution of particles to the hybrid energy eqn (4). Here, we prefer the direct route of matching chemical potentials in a mixed system or pressures in pure monomeric systems of particles and field. The second condition ensures that replacing all particles by a single field reproduces the density fluctuations that are known to be sufficiently captured by the (soft-core) particle model.¹⁷ Pressure effects by the solvent on the membrane were found to be absent for systems where the particle self-repulsion a_{ii} is the same for all species, which is the case here, leading to the conclusion that such a system is more like a one-component (water) system than a multi-component system.²² This could be expected, since the pressure will mainly depend on the density. For this reason, we conclude that mixed systems with a fixed density and only excluded volume interactions will be mechanically stable when brought into contact, if the pressure in the pure systems is sufficiently matched.

It is worthwhile to note that different routes, *i.e.* *via* pressure or chemical potential, will not necessarily yield exactly the same result. This asymmetry is caused by the Harmonic equation of state for the pressure, that is exact in the case of DDFT, as a consequence of the chosen Helfand term, and semi-empirical for the particle model. The few percent deviations for the particle case are enough to shift chemical potentials, and render it impossible to exactly match the pressure and the chemical potential simultaneously. As a solution, one may consider replacing the Helfand term in DDFT by one containing a cubic term in the density and use the additional coefficient in a fitting procedure. Nevertheless, we consider this issue not very important at this stage and only report and discuss the results for the two different routes.

Equation of state for the pressure of the field

For a monomeric field, the density of the field free energy functional F^{f} is¹⁶

$$f^{\text{f}}(\mathbf{r}) = \rho_{\text{f}}(\mathbf{r}) \ln \rho_{\text{f}}(\mathbf{r}) + \frac{\kappa_{\text{H}}}{2} \rho_{\text{f}}(\mathbf{r})^2 \quad (8)$$

where $\rho_{\text{f}}(\mathbf{r})$ is the density field for solvent monomers and κ_{H} is the Helfand compressibility parameter. For simplicity, we have omitted the reference field in the compressibility term,¹⁶ since it gives rise to a constant and homogeneous contribution to the chemical potential. In the absence of particles, *i.e.* with coupling parameters $c = 0$, the only non-zero term in the hybrid energy functional eqn (4) is the free energy $F^{\text{f}}[\rho_{\text{f}}]$. The hybrid method reduces to the standard DDFT theory, and the pressure p_{f} is given by²³

$$p_{\text{f}} = - \left(\frac{\partial F^{\text{f}}}{\partial V} \right)_{n,T} = \rho_{\text{f}} + \frac{\kappa_{\text{H}}}{2} \rho_{\text{f}}^2 \quad (9)$$

where $\rho_{\text{f}} = n/V$ (a homogeneous ideal gas). Comparing eqn (9) and (7), it is easy to see that the equivalent equation of state for the pressure is obtained by setting $\kappa_{\text{H}} = 2\alpha a_0$, provided that we choose $\rho_{\text{p}} = \rho_{\text{f}}$. Consequently, the Helfand (field) compressibility parameter corresponding to $a_0 = 25$ is $\kappa_{\text{H}} = 5.0$. The alternative route, directly *via* the isothermal compressibility of water at room temperature $\kappa^{-1} = 1 + \kappa_{\text{H}}\rho_{\text{f}} = 16$, provides the same value $\kappa_{\text{H}} = 5.0$ for $\rho_{\text{f}} = 3$.

This matching procedure suggests precision, but the procedure for calculating the DPD pressure deserves a closer examination. The α considered in eqn (7) is the *asymptotic* value for $(p - \rho_{\text{p}}k_{\text{B}}T)/(\alpha_0\rho_{\text{p}}^2)$, see Fig. 4 in ref. 17 and the authors claim that this asymptotic value is valid for $\rho_{\text{p}} \geq 3$. Nevertheless, a closer look at this figure shows that the curve is monotonically increasing for the whole ρ_{p} -range. One could argue that the observed density dependence of α , which becomes prominent for low ρ_{p} , stems from the selection of a fixed cutoff distance r_{c} or a density-dependent overlap probability. The same argument was previously used to define a density dependent cutoff distance to render DPD scalable.²⁴ The actual pressure in the soft-core particle system is thus somewhat lower than suggested by eqn (7). Although there are good reasons for considering a_0 that are independent of the particle density, our pressure matching procedure should consider the real pressure, *i.e.* we should use $\alpha(\rho)$ instead of a constant α . From $\alpha(3) \approx 0.09$, determined using the curve of Groot and Warren,¹⁷ we obtain $\kappa_{\text{H}} = 2\alpha(3)a_0 \approx 4.5$ for $\rho_{\text{p}} = \rho_{\text{f}} = 3$. The route *via* the isothermal compressibility of water provides

$$\kappa^{-1} = \left(\frac{\partial p_{\text{p}}}{\partial \rho_{\text{p}}} \right)_T = 1 + \frac{\partial \alpha(\rho_{\text{p}})}{\partial \rho_{\text{p}}} a_0 \rho_{\text{p}}^2 + 2\alpha(\rho_{\text{p}}) a_0 \rho_{\text{p}} \quad (10)$$

and inserting $\rho_{\text{p}} = \rho_{\text{f}} = 3$, $a_0 = 25$ and $\partial \alpha / \partial \rho_{\text{p}} \approx 0.007$ and $\alpha \approx 0.09$ shows that equal isothermal compressibility is obtained for $\kappa_{\text{H}} \approx 4.55$, very close to the value determined *via* pressure matching. The alternative route, matching the excess chemical potentials for a mixed system of monomeric particles and fields numerically, provides $\kappa_{\text{H}} \approx 4.9$. It is clear that κ_{H} should be chosen in the small range [4.5, 4.9] and that the actual value

depends on the property that one would like to match. Since $a_0 = 25$ is determined *via* the isothermal compressibility, we set $\kappa_H = 4.6$ in the remainder.

The good correspondence between the theoretical mean field value and the DPD simulations should be no surprise: it has since long been known that the soft potentials render DPD almost exactly mean field, where the correspondence becomes better the higher the density, *i.e.* the more soft particles will overlap.²⁵ In fact, in the well-known Groot–Warren parametrization of the a -parameter (ref. 17, more on that below), one makes use of the close agreement between Flory–Huggins and DPD simulations in calculating phase diagrams of polymer blends. Phase boundaries in block copolymer melts were also found to coincide.²⁶

Mixed systems: relating coupling parameters to Flory–Huggins χ and DPD a parameter

It seems natural to adapt the DPD concept and separate the coupling parameter c_{ik} into two contributions c_0 and Δc_{ik} , representing the excluded volume and cohesive particle–field interactions, respectively. Determining c_0 directly by analytical means is complicated by the heterogeneity of the system. Nevertheless, we can analyze the pressure in a mixed monomeric particle and field system when considering the limiting case of sufficiently high particle concentration. We will validate the generality of these findings by numerical means later on.

The starting point is a mixture of a monomeric particles and field, with a single coupling parameter c . We introduce a density of particles

$$\sum_k K(\mathbf{r} - \mathbf{r}_k) = \rho_p(\mathbf{r}) \quad (11)$$

and use as a key assumption that the particle density is high enough to consider eqn (11) as a stationary field, owing to sufficient overlap of individual smoothed particle fields. In that case, since the coupling chemical potential $\mu^{\text{pf}}(\mathbf{r}) = c\rho_p(\mathbf{r})$ does not depend on fluctuations in the particle subsystem, the field also does not change with time. In particular, the coupling energy and the free energy of the field subsystem provide a constant contribution to the ensemble-average of the hybrid energy eqn (4), given by

$$\langle F[\{\mathbf{r}_k\}, \{\rho_f\}] \rangle = \langle E^{\text{P}}(\{\mathbf{r}_k\}) \rangle + F^{\text{f}}[\rho_f] + F^{\text{pf}}(\rho_p, \rho_f) \quad (12)$$

The pressures for the field and coupling term, p_f and p_c , can be calculated in the standard (field) way, using the derivative with respect to volume, equivalent to eqn (9). For the pressure due to the particle subsystem, we use the phenomenological expression eqn (7). The general expression for p_f and p_c is given by

$$p_f = \frac{n_f}{V} + \frac{\kappa_H}{2V} \int_V \rho_f(\mathbf{r})^2 d\mathbf{r} \quad (13)$$

$$p_c = \frac{c}{V} \int_V \rho_p(\mathbf{r})\rho_f(\mathbf{r}) d\mathbf{r}$$

where we have used the assumption that $\rho_f(\mathbf{r}) + \rho_p(\mathbf{r}) = \bar{\rho} = (n_p + n_f)/V$, with n_p and n_f the total number of particles in the

particle and field representation respectively, for deriving the expression for the coupling pressure. Next, we consider the case that particles and fields are homogeneously distributed, *i.e.* $\rho_f(\mathbf{r}) = n_f/V$ and $\rho_p(\mathbf{r}) = n_p/V$. Insertion into eqn (13) gives rise to the simple expression

$$p_f + p_c = \rho_f + \frac{\kappa_H}{2}\rho_f^2 + c\rho_p\rho_f. \quad (14)$$

Combining eqn (14) and (7), we obtain the total pressure for the hybrid system

$$p = p_p + p_f + p_c = \rho_p + \alpha a_0 \rho_p^2 + \rho_f + \frac{\kappa_H}{2}\rho_f^2 + c\rho_p\rho_f$$

$$= \rho_p + \rho_f + \frac{\kappa_H}{2}(\rho_p^2 + \rho_f^2) + c\rho_p\rho_f. \quad (15)$$

where we exploited the relationship $\kappa_H = 2\alpha a_0$ for the conversion of excluded volume interactions in pure particle and field systems. We note that this relationship is independent of particular values of κ_H and a_0 . Rewriting eqn (15) as

$$p = \rho_p + \rho_f + \frac{\kappa_H}{2}(\rho_p + \rho_f)^2 + (c - \kappa_H)\rho_p\rho_f \quad (16)$$

shows that the equation of state for the total pressure of the hybrid system adapt the usual form, *i.e.* quadratic in $\bar{\rho}$, only for $c = \kappa_H = 2\alpha a_0$.

One can interpret the result eqn (16) by considering the pressure contribution p_{coh} due to F^{coh} , the mean-field cohesive interactions in the DDFT model.¹⁶ For the situation considered so far, a single field of type I , the cohesive term vanishes due to $\chi_{II} = 0$ and this contribution can be disregarded. For a blend of two monomer types, I and J , in the field description that are fully *miscible*, *i.e.* $\rho_f(\mathbf{r}) = \rho_I$ and $\rho_f(\mathbf{r}) = \rho_J$, the pressure contribution is given by

$$p_{\text{coh}} = \chi_{IJ}\rho_I\rho_J \quad (17)$$

with $\chi_{IJ} = \chi$ the usual Flory–Huggins parameter. We note that the monomers are miscible for $\chi < 2$ and that by convention $\chi_{II} = \chi_{JJ} = 0$. We can now compare the total pressure p_f for this system,

$$p_f = \rho_I + \rho_J + \frac{\kappa_H}{2}(\rho_I + \rho_J)^2 + \chi\rho_I\rho_J, \quad (18)$$

to the pressure in the mixed system eqn (16). Evidently, the representations are completely equivalent in terms of pressure if we identify an ‘effective’ Flory–Huggins parameter, for the mixed system of particles and field, as

$$\chi = c - \kappa_H \quad (19)$$

Moreover, as the non-ideal part of the DDFT free energy reduces to the compressibility term F^{comp} for $\chi = 0$, we find by equivalence that $c_0 = \kappa_H$ accounts for the excluded volume interactions in the hybrid model. Since κ_H was determined for $\rho_f = 3$ in the previous subsection, we need to account for an average field concentration $\bar{\rho} = \sum_I \bar{\rho}_I$, with

$$\bar{\rho}_I = \frac{1}{V} \int_V \rho_I(\mathbf{r}) d\mathbf{r}, \quad (20)$$

that deviates from unity. Simple scaling analysis for the particle volume in DDFT shows that the standard Flory–Huggins

parameter scales with $1/\bar{\rho}$. Consequently, eqn (19) in the most general form is given by

$$\frac{\chi}{\bar{\rho}} = c - \kappa_H \rightarrow \chi = \bar{\rho}(c - \kappa_H) \quad (21)$$

We note that homogeneity is a sufficient but not a necessary condition for the derivation of this equivalency. The present result can rather straightforwardly be extended to the case of inhomogeneous fields $\rho_p(\mathbf{r})$ and $\rho_f(\mathbf{r})$, provided that the spreading factors in the kernels in F^{coh} and F^{fp} are matched.

To relate the coupling parameters directly to soft-core particle interactions, we use the effective mapping between Flory–Huggins $\chi > 2$ and Δa determined by Groot and Warren,¹⁷

$$\begin{aligned} \chi &= (0.286 \pm 0.002)\Delta a & \rho_p &= 3 \\ \chi &= (0.689 \pm 0.002)\Delta a & \rho_p &= 5 \end{aligned} \quad (22)$$

Combining eqn (21) and (22) for $\rho_p = 3$, we end up with the desired relationship

$$0.286\Delta a = 3(c - 4.6) \quad (23)$$

Dynamics

The hybrid free energy eqn (4) is minimized *via* a set of stochastic Langevin equations for particles and fields, much in the same spirit as the procedure for pure fields in DDFT. The fluctuating/noise terms in the Langevin equation for the field and BD for the particles can be chosen independently.²⁷ The resulting fully diffusive pathway mimics the experimental structure evolution in the case that hydrodynamics does not play an important role. An illustration of such a situation is a (viscous) ABA block copolymer thin film, where the simulated (by DDFT) and experimental pathways of a phase transition matched reasonably well, even in detail.²⁸ For membrane forming systems, field-based models with the same dynamic description were shown to reproduce all distinctive structures in the experimental sequence from a homogeneous mixture to closed vesicles.^{29–31} From a quantitative point of view, however, the literature shows that proper coarse-grained modeling of lipid membrane dynamics is a complex task. Three sources of dissipation are associated with membrane motion and should be accounted for: solvent and membrane viscous dissipation, and a sliding friction between the leaflets, which occurs whenever there is membrane curvature. The relatively high viscosity within the membrane ($\sim 10^3 \eta_w$, with η_w the viscosity of water) suggests that momentum transfer is sufficiently damped, *i.e.* that Brownian motion suffices to capture the translational diffusion of lipids within each of the leaflets. However, the longer-range interactions due to momentum transfer with the surrounding solvent are known to be particularly important for membrane formation and remodeling, and speed up collective motion in these phenomena. Coarse-grained MD with implicit solvent represents an intermediate in this context, as it neglects momentum transfer between solvent and membrane but accounts for these contributions within the membrane. For the moment, we are tied to a purely diffusive description and

acknowledge this limitation. The introduction of Lattice Boltzmann in this new framework will resolve this issue, and will be considered at a later stage, as mentioned in the introduction.

Particle positions are updated according to position Langevin dynamics,

$$d\mathbf{r}_k = M_k \mathbf{f}_k dt + \mathbf{r}_k^R \quad (24)$$

describing particle diffusion in a viscous polymeric medium (overdamped limit), where M_k is the constant mobility coefficient for particle k . In contrast to DPD, the friction force on a particle does not depend on surrounding particles, but is given by

$$\mathbf{f}_k^f = -\mathbf{f}_k \frac{\partial \mathbf{r}_k}{\partial t} \quad (25)$$

with a friction coefficient \mathbf{f}_k related to the diffusion constant D_k by the Einstein relationship $\mathbf{f}_k = k_B T / D_k$. The mobility coefficient is defined as $M_k = \mathbf{f}_k^{-1}$, which can be rewritten as $k_B T M_k = D_k$. A standard choice is $D_k = D$ and fields ρ_l are treated as independent variables. The first term in eqn (24) is the drift term, with a force

$$\mathbf{f}_k = -\frac{\partial F}{\partial \mathbf{r}_k} = -\frac{\partial E^p}{\partial \mathbf{r}_k} - \frac{\partial F^{\text{pf}}}{\partial \mathbf{r}_k} = \mathbf{f}_k^{\text{nb}} + \mathbf{f}_k^{\text{pf}}, \quad (26)$$

that gives rise to a reduced F , independent of the temperature T . It comprises forces due to particle–particle (\mathbf{f}_k^{nb}) and particle–field (\mathbf{f}_k^{pf}) interactions. The forces due to particle–particle interactions are the standard ones from DPD, notably the conservative forces due to the non-bonded potentials eqn (2) given by

$$\mathbf{f}_k^{\text{cons}} = \sum_{r_{kl} < 1} a_{kl} (1 - r_{kl}) \hat{\mathbf{r}}_{kl} \quad (27)$$

where $\hat{\mathbf{r}}_{kl}$ is the unit vector pointing from particle l to particle k , plus additional intramolecular forces due to bonded interactions, like spring, angle and torsion forces. The second term in eqn (26) is a coupling force due to particle–field interactions, given by

$$\begin{aligned} \mathbf{f}_k^{\text{pf}} &= -\sum_I c_{Ik} \int_V \frac{\partial K(\mathbf{r} - \mathbf{r}_k)}{\partial \mathbf{r}_k} \rho_I(\mathbf{r}) d\mathbf{r} \\ &= \frac{2}{\sigma^2} \sum_I c_{Ik} \int_V (\mathbf{r} - \mathbf{r}_k) K(\mathbf{r} - \mathbf{r}_k) \rho_I(\mathbf{r}) d\mathbf{r} \end{aligned} \quad (28)$$

or

$$\mathbf{f}_k^{\text{pf}} = -\sum_I c_{Ik} \int_V K(\mathbf{r} - \mathbf{r}_k) \nabla \rho_I(\mathbf{r}) d\mathbf{r} \quad (29)$$

via integration by parts. In our simulations, the coupling parameters c_{Ik} are positive, and the coupling force points to the direction of the fastest decrease in field density. To conclude, the second term in eqn (24) is the standard random displacement

$$\mathbf{r}_k^R = \sqrt{2k_B T M_k} dW_k(t) \quad (30)$$

of Brownian dynamics (BD). In particular, $dW(t)$ is a multivariate Wiener process with $\langle dW_i(t) dW_j(t) \rangle = \delta_{ij} dt$. Numerical tests

showed that the fluctuating contributions from the (solvent) field allow for omitting this random term in practice. However, athermal particle evolution comes with a high risk of particle freezing, especially in particle-rich domains that contain (almost) no field, so we decided to include a random term.

For the evolution of the field subsystem, we can use any of the available DDFT schemes. They differ only in the model for the local kinetics, reflected in the particular diffusion operator. We choose external potential dynamics³²

$$\frac{\partial U_I}{\partial t} = -D_I \nabla^2 \mu_I + \eta_I \quad (31)$$

where D_I is a diffusion coefficient for the I -type field, η_I is an appropriately chosen noise field and U_I is the external potential field conjugate to the density field ρ_I . The densities and external potentials are bijectively related, allowing us to freely exchange between external potentials and densities. The intrinsic chemical potentials follow from eqn (4)

$$\mu_I = \frac{\delta F}{\delta \rho_I} = \frac{\delta F^f}{\delta \rho_I} + \frac{\delta F^{pf}}{\delta \rho_I} \quad (32)$$

where the first term is given by the standard chemical potential in DDFT.¹⁶ Hence, particles influence the field dynamics eqn (31) *via* the coupling chemical potential

$$\mu_I^{pf} = \frac{\delta F^{pf}}{\delta \rho_I} = \sum_k c_{Ik} K(\mathbf{r} - \mathbf{r}_k). \quad (33)$$

For a monomeric field, the intrinsic chemical potential becomes

$$\mu_I = \ln \rho_I(\mathbf{r}) + \kappa_H \rho_I(\mathbf{r}) + \sum_k cK(\mathbf{r} - \mathbf{r}_k) \quad (34)$$

Results and discussion

This article focusses on the parametrization and the results will be limited to a proof of principle for our hybrid method. First, we challenge the analytically derived relationship eqn (23), between the hybrid coupling and DPD a -parameters, by solubility calculations for a mixed system of monomeric particles and field. Consequently, we compare the structural properties of membranes in DPD and the hybrid method, focussing on the membrane thickness and particle density profile within the membrane, in order to see if these properties are sufficiently reproduced. Finally, we use large-scale simulations to study the spontaneous assembly from a homogeneous lipid-solvent mixture and the repair mechanism for a large pre-assembled vesicle that has been punctured. We start by considering the simulation setup and parameters.

Simulation setup

Simulations were performed in a $V = L_x \times L_y \times L_z$ simulation volume, with L_i ($i \in \{x, y, z\}$) the length in each of the three Cartesian directions in units of r_c , the cut-off distance for the particle interactions. Field values were calculated and stored on an equidistant grid with discretization distance r_c , *i.e.* $\rho(i\mathbf{r}_c, j\mathbf{r}_c, k\mathbf{r}_c) = \rho_{i,j,k}$ for $i, j, k \in \mathbb{N}$, but the underlying molecular

representation is essentially not restricted to the grid. The particle description is mesh-free, but a computational grid is introduced for efficient computation of conservative forces, with an offset of $r_c/2$ with respect to the field grid. Domain decomposition was used for parallelization, and periodic boundary conditions are employed along all Cartesian directions, for both field and particles.

We consider the $H_3(C_4)_2$ representation for a DMPC lipid of Shillcock and Lipowsky.¹¹ Particles are assumed to have identical mass m (in kg) and radius, which are equal to the cut-off distance r_c (in m). For consistency and ease of notation, we introduce dimensionless parameters. For the conservative forces, they are given by $l_0^* = l_0/r_c$, $k_2^* = k_2 r_c^2/k_B T$, $k_3^* = k_3/k_B T$ and $a_{ij}^* = a_{ij} r_c/k_B T$. Other dimensionless DPD parameters are the density $\rho^* = \rho r_c^3$, position $\mathbf{r}^* = \mathbf{r}/r_c$, velocity $\mathbf{v}^* = \mathbf{v} \sqrt{m/k_B T}$, time $t^* = t \sqrt{k_B T/mr_c^2}$ and friction coefficients $\gamma_{ij}^* = \gamma_{ij} \sqrt{r_c^2/mk_B T}$. The latter are related to the noise coefficients σ_{ij} by the fluctuation-dissipation theorem as $\sigma_{ij}^2 = 2\gamma_{ij} k_B T$ and we find $(\sigma_{ij}^*)^2 = 2\gamma_{ij}^*$. All discussed parameter values in the remainder are dimensionless, so we neglect the asterix.

A lipid consists of three head (H) particles and two hydrocarbon (C) tails of four particles each. Each C particle represents 3.5 CH_2 groups. For convenience later on, the two terminating particles are denoted by the letter E, but are further undistinguishable from C particles, and are given a different color in all figures in the remainder. Each of the two tails is connected to a different head (H) particle. Connectivity is facilitated by harmonic springs, with an equilibrium length $l_0 = 0.5$ and spring constant $k_2 = 128$, and stiffness is induced by an angle potential ($\phi_0 = 0$) with bending constant $k_3 = 20$. Due to the monomeric nature of the water particles (denoted by W) our mapping procedure is only used to determine the coupling c_{HW} and c_{CW} parameters. Table 1 recapitulates the values of $a_{ij} - a_0 = \Delta a_{ij}$ used by Shillcock and Lipowsky. The interaction between like-particles $a_{ii} = a_0$ was determined from the isothermal compressibility of water, *i.e.* $a_0 = 25$ for a density $\rho = 3$.

The time step Δt in DPD is a compromise between efficiency and the equilibrium condition. Groot and Warren showed that significant deviations of the observed temperature from the input T arise for both the Euler and Verlet integration schemes if this time step is chosen too large.¹⁷ Moreover, the temperature relaxation rate was shown to depend on the noise amplitude σ , and, guided by their numerical evaluation, reasonable values were determined as $\Delta t = 0.04$ and $\sigma = 3$. We note that updating the forces and velocities consistently²¹ is the proposed solution for this limitation, but such an algorithm was not considered here. For the Verlet scheme used in our DPD implementation, the default values are $\Delta \tau = 0.02$ and $\sigma_{ij} = 3$. In Shillcock and

Table 1 The interaction parameter Δa_{ij} used in Shillcock and Lipowsky¹¹

| Δa_{ij} | $j = \text{H}$ | $j = \text{C}$ | $j = \text{W}$ |
|-----------------|----------------|----------------|----------------|
| $i = \text{H}$ | 0 | 25 | 10 |
| $i = \text{C}$ | 25 | 0 | 50 |
| $i = \text{W}$ | 10 | 50 | 0 |

Lipowsky's work, the time step is not discussed and the friction coefficients γ_{ij} were chosen in agreement with $\sigma_{ij} = 3$ ($\gamma_{ij} = 4.5$), except for $\gamma_{HC} = 9$ and $\gamma_{CW} = 20$.¹¹ Although the particular choice of γ_{ij} is irrelevant for the equilibrium behavior, as long as the system is properly thermostatted, we adapted these values for γ_{ij} in our DPD simulations.

The dimensionless variables and parameters for the field part of the hybrid model were previously published.¹⁶ We follow the evolution of number density fields $\rho^*(\mathbf{r}) = \nu\rho(\mathbf{r})$, using an external potential $U^*(\mathbf{r}) = U(\mathbf{r})/k_B T$ and chemical potential $\mu^*(\mathbf{r}) = \mu(\mathbf{r})/k_B T$, where ν is the particle volume (for simplicity, we consider $\nu \sim r_c^3$). Apart from a scaling factor in the noise amplitude, $\Omega = 100$, input parameters are the Flory–Huggins interaction $\chi = 0$, the step size $\Delta\tau = D^*\Delta t^*$, with time $t^* = t/t_{sc}$ and diffusion coefficient $D^* = Dt_{sc}/r_c^2$, and the compressibility parameter $\kappa_H^* = \kappa_H\nu/k_B T$. The time scale t_{sc} (s) can be arbitrarily chosen. In the particle description, the same parameters as above are used for the conservative force, for positions $\mathbf{r}^* = \mathbf{r}/r_c$ and step size $\Delta\tau = D_k^*\Delta t^*$, with time $t^* = t/t_{sc}$ and diffusion coefficient $D_k^* = k_B T M_k t_{sc}/r_c^2$. Default values for the diffusion coefficients are $D^* = 1.0$ and $D_k^* = 0.04$. We introduce an additional scaling factor $\sqrt{T^*}$ (default: $T^* = 1$) in the noise amplitude, similar to the field case. The hybrid part is made dimensionless by $\sigma^* = \sigma/r_c$, $c_{Ik}^* = c_{Ik}/k_B T r_c^3$ and $K^*(\mathbf{r}) = K(\mathbf{r})r_c^3$, where we have set the particle volume $\nu_k = \nu$. In all simulations, we use a spread of the Gaussian kernel $\sigma = 0.8$. We employed a Crank–Nicolson scheme (with CN parameter $\gamma = 0.5$) for the field updates and an explicit Euler scheme for the particle updates. We introduce a possibility of desynchronization: particle positions and field values are not necessarily updated every time step. The frequency of field updates, *i.e.* the number of time steps between a field update, is denoted as f_{up} .

Preparation of the starting structure

Depending on our objective, we either start our hybrid simulations from a homogeneous situation or a pre-assembled membrane. Unless mentioned otherwise, the solvent is introduced as a spatially homogeneous field $\rho(\mathbf{r}) = N_w/N$, where $N_w = N - 11N_l$ (each lipid contains 11 particles) is the number of water particles that $\rho(\mathbf{r})$ represents and $N = \rho L_x L_y L_z$, the total number of particles in a full particle representation. Homogeneous conditions are imposed by setting $U(\mathbf{r}) = 0$ for the solvent field and random initial positions for the lipid chains. Pre-assembled flat or curved membranes were prepared *via* a more involved procedure. Initially, the simulation volume is filled with $N_l = N_{l,i} + N_{l,o}$ lipids. The number of lipids $N_{l,i}$ and $N_{l,o}$ in the inner and outer membrane leaflets are calculated based on the desired area per lipid $A_j/N_{l,j}$ ($j = i$ or o), where A is the dimensionless area of an unperturbed leaflet. Subsequently, both lipid portions are distributed over each of the leaflets according to the lipid ratio, at random positions, under the constraint that heads face the lipid–water interface and all terminating *E* particles are part of a thin region (a shape field *a*) along the midplane between the two leaflets. This membrane is relaxed in several consecutive steps: (a) lipids are first equilibrated without solvent for $c_{Ea} = -75$ ($c_{Ca} = c_{Da} = 0$) and 10^3

steps, assuring the membrane integrity by the strong attraction of the tail *E* particles to the *a* region, (b) a homogeneous solvent field is introduced with $\chi_{sa} = 10$ and the system is equilibrated for 10^3 steps to let the solvent field diffuse away from the *a* region around the midplane, (c) the solvent field is equilibrated for another 10^4 steps, using a Picard method, for stationary particles, (d) the constraint on particles is released and the system is equilibrated 10^2 steps, and (e) the interaction c_{Ea} is slowly increased to $c_{Ea} = -20$ ($\Delta c = 2$ every 200 steps). Finally, the *a* field is removed and the simulation is started with this structure.

Solubility calculations

Using the analytical relation eqn (21) derived for the limiting case

$$c_{ij} = 0.095\Delta a_{ij} + 4.6 \quad (35)$$

we obtain $c_{HW} = 5.55$ and $c_{CW} = 9.37$. To test relation eqn (21), we consider the partitioning in a system consisting of monomeric (A) field and (B) particles, for $\kappa_H = 4.6$ and varying c_{AB} . At the start of the simulation, the simulation volume of $L_x \times L_y \times L_z = 160 \times 10 \times 10$ is occupied by pure phases of particles and field, in equal amounts, which are into contact and can freely diffuse. Simulations were continued for an additional 2000 time steps after equilibrium was reached, which is monitored *via* the hybrid free energy. Equilibrium profiles along the *x*-direction for the fields and particles (after particle-to-field mapping) were obtained by averaging over orthogonal directions and the last 2000 time steps. Single values for the field concentration ρ in the particle phase as well as the total concentration $\bar{\rho}$ were determined by spatial averaging over the region of $2k + 1$ ($k \leq 15$) grid points, in the middle of the particle-rich phase centered around $x = 80$. We found that $\phi = \rho/\bar{\rho}$ is insensitive to the width k of the domain used for spatial averaging. Inserting ϕ into the expression for the equilibrium volume fraction in a binary system in Flory–Huggins theory¹⁷

$$\chi^p = \frac{\ln[(1 - \phi)/\phi]}{1 - 2\phi} \quad (36)$$

relates the Flory–Huggins χ and c_{AB} ($N = 1$). Relation eqn (36) is intrinsically symmetric in particles and fields, but we selected the field in the particle phase, as the combination of slow diffusion and low particle concentrations in the field phase, especially for higher coupling c_{AB} , gives rise to rather poor statistics. For similar reasons, we restricted the coupling range to $c \leq 10$. Fig. 2 shows both the analytic estimate of χ (solid line) and χ^p (+) for varying $5 \leq c_{AB} \leq 10$. The values of χ^p are slightly below the analytical estimates, except for $c_{AB} = 5$, but agree quite well for the whole range. Close to the critical point $\chi = 2$ *i.e.* for $c_{AB} \approx 5$, we cannot expect the mean-field expression to hold.¹⁷ In the remainder, we therefore rely on the analytical dependence, and consider $\kappa_H = 4.6$, $c_{HW} = 5.55$ and $c_{CW} = 9.37$. We note that, owing to the strong particle–water repulsion for the lipid tail particles, there is a substantial energetic barrier for membrane lipids to ‘evaporate’ into the water phase and for the water field to enter the membrane core. Once lipid domains are

formed, the simulation volume will thus remain separated in particle- and field-rich domains.

Membranes properties

Next, we consider the structural properties of a membrane that is pre-assembled along the x - z direction in a simulation volume of $8 \times 16 \times 8$. We focus on a membrane that is close to the tensionless state. Using the results of Shillcock and Lipowsky, such a membrane is obtained for an (projected) area per lipid $A/N = 1.26$,¹¹ or, using the number of lipids per unit area lpa instead, for $\text{lpa} = 0.79$. As a result, each leaflet contains $\text{lpa} \times 8 \times 8 = 50$ lipids and the total number of lipids $N_l = 100$, which is rather small compared to the 1685 lipids considered previously.¹¹ Our simulation volume was particularly chosen to reduce the role of membrane shape fluctuations, see Fig. 1, and the averaged profiles in Fig. 3. Detailed analysis of simulation results for slightly larger volumes ($10 \times 20 \times 10$) showed that the averaged profile is much more sensitive to these shape fluctuations than to a (small) variation of the coupling parameters.

After equilibration, hybrid simulations were performed for 2×10^5 time steps, using default values for the time increment, diffusion coefficients and $f_{\text{up}} = 10$. Collecting snapshots every 500 time steps, we calculated the average density profiles perpendicular to the membrane, by averaging particle densities over thin slices (of width $1/4$) along the x - z direction and over the available snapshots. In addition, we averaged over simulated pathways for 40 different noise seeds. As a reference, we also performed DPD simulations using an equivalent membrane preparation procedure and the same averaging for the simulation part. Simulation snapshots for both models at the end of the simulations are shown in Fig. 1 and averaged particle number density profiles in Fig. 3.

The profiles for the head (H) and tail (C) particles in the structures obtained using the hybrid method (solid lines) and

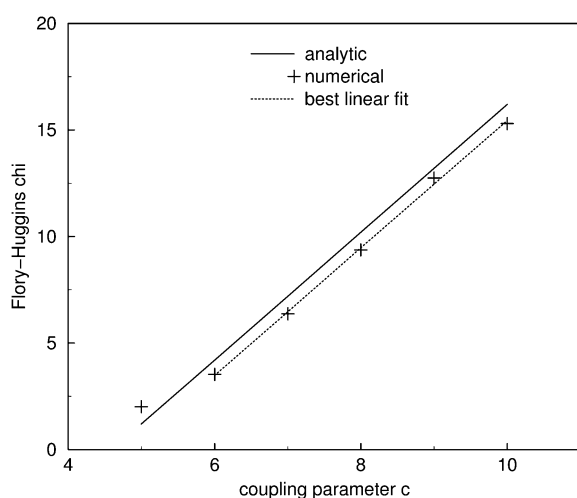


Fig. 2 The relation between Flory-Huggins χ (vertical axis) and coupling parameter c (horizontal axis). Solid line: analytic estimate $\chi = 3(c - \kappa) = 3(c - 4.6)$. Symbols (+): values for χ determined from simulations. Dotted line: best linear fit $\chi = 2.99(c - 4.83)$ for the numerical data in the range $6 \leq c \leq 10$, away from the critical point.

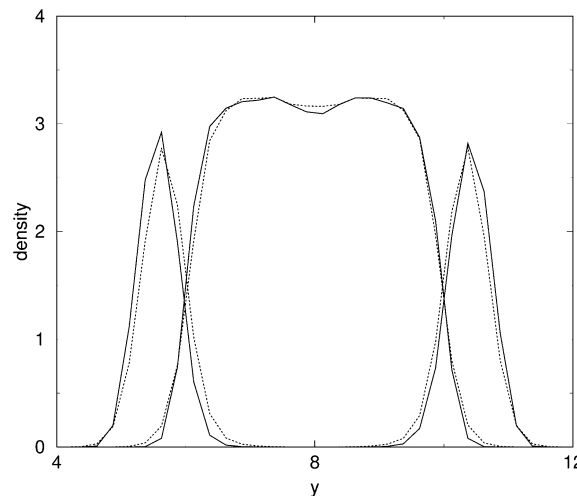


Fig. 3 Average particle number densities for the H (head) and C (tails) particles perpendicular to the membrane (along the y -axis), averaged along the x and z axes and over 10^3 simulation snapshots. The solid line is the result for the hybrid method and the dashed line the result for DPD.

DPD (dashed lines) in Fig. 3 are in good agreement. In particular, the membrane thickness is identical in both models. This shows that the origin of membrane formation and stability, the hydrophobic interactions between the lipid head and surrounding water, are equally well captured by the hybrid and DPD descriptions. Inside the membrane, lipids are disordered within each leaflet for both simulation methods, as can be seen from the simulation snapshots in Fig. 1, and leaflets are not very interdigitated, in agreement with fluid-like behavior of the membrane. Although density profiles for $\text{H}_3(\text{C}_4)_2$ membranes were not explicitly considered in the earlier study,¹¹ the dip in the C-particle density profile at the midplane of the bilayer was previously observed for HC_6 lipids and reflects the enhanced conformational sampling of the terminal particles. This dip is somewhat enhanced in the hybrid model.

We shortly identify factors that are important for the membrane properties. We start with the kinetic description. Although the choice of the dynamic model is irrelevant for the equilibrium structure, the averaging procedure is sensitive to bilayer shape fluctuations and to the lipid exchange rates between leaflets,¹¹ which were earlier shown to be anomalously high for DPD with our parameter set.³³ These effects are still rather insignificant, but the degree to which they change the details of the average density profiles depends on the kinetic description. The enhanced mass transport in DPD has the effect of smearing, which could be the cause for the different dip depth. Also the representation of the solvent is different. In DPD, the probability of solvent particles entering the membrane is very low, owing to a large energetic penalty. In the hybrid model, a residual solvent field is *always* present inside the membrane, independent of the coupling parameter, although the tiny amount for our parameters is unlikely to have much effect on the membrane structure. Parametrization and implementation are the two remaining factors. We used the pressure for estimating the Helfand parameter $\kappa_H = 4.6$ in the field

model, but the excess chemical potential provides $\kappa_H = 4.9$. Our simulations showed that such small variations have no significant effect. Finally, the combination of grid-based field and off-grid particle representations should be handled with care. The design of optimal discrete integral operators for this case is a considerable theoretical challenge and warrants a separate publication. For the selected discrete 27 point representation, H particles close to the water–lipid interface experience a weak tendency to align with the computational field grid (see Appendix A for a detailed analysis). From Fig. 3 we may conclude that grid artifacts do not seriously affect the particle density profile. However, we should note that the equilibrium membrane thickness roughly coincides with an integer number of grid spacings.

Analysis of membrane surface tension for the hybrid model is complicated by the lack of a straightforward procedure for calculating this tension in the mixed representation. Application of another standard method, the well-known Helfrich analysis of membrane shape fluctuations, is prohibited by our dynamic model that does not capture the long-range correlations that are responsible for these motions. Instead, we attempted to rigorously calculate the surface tension *via* an alternative approach of assembling a membrane between two frozen colloids and determining the average force per unit area on the colloids by simulation (we will use the term ‘colloid’ here and below to denote a collection of particles with frozen internal degrees of freedom, see Fig. 4), adopting the averaging steps for the membrane profile. We concentrated on the conclusions that can be drawn from this study and chose to only discuss (and not show) simulation data. The results of the DPD simulations for this setup match reasonably well with previously published surface tension results for membranes that are constrained by periodic boundary conditions at both sides,¹¹ although the match is not perfect. We find that the slope of the surface tension *versus* lpa for the hybrid model is comparable to the one obtained by DPD, but that the location of the tensionless state differs. Optimization, using equal increments for both couplings, provided a good match for only slightly higher coupling parameters. Nevertheless, we concluded that this approach is not robust enough for a quantitative comparison and/or fitting procedure. In particular, the area per lipid for a tensionless state varies considerably with the rather arbitrary choices of several other parameters, such as the total simulation volume, the colloid–lipid interactions and the size of the membrane patch, as well as the choice to include or exclude force contributions due to the solvent. The sensitivity of surface tension to membrane preparation, in particular to the number of lipids per unit area, was earlier observed and reflects the large area stretch modulus for these bilayers.¹¹

Large scale simulations

We conclude with proof-of-principle simulations that focus on collective structuring or restructuring phenomena on large scales, *i.e.* on the scale of experimental liposomes. We stress again that in-depth analysis of the simulation results is not the primary goal of this study. Instead, we focus on the performance

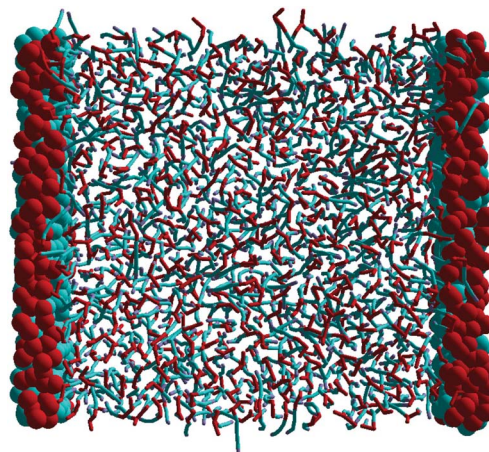


Fig. 4 Top view of the starting structure for the force calculations (solvent not shown). The membrane was prepared in a smaller volume with periodic boundary conditions. Subsequently, one dimension was increased, and lipids close to the two membrane edges were frozen into colloids. Frozen and unconstrained lipids are represented differently for clarity. In the unconstrained direction, the membrane is stabilized by periodic boundary conditions. Blue: tail (C) particles and red: head (H) particles.

of two standard cases, lipid self-assembly from a homogeneous mixture and healing of a preassembled but punctured vesicle, and use these results to illustrate the limitations and advantages of the new method for future application.

Before discussing the results, we shortly review the basic limitations of simulating liposome formation from a homogeneous mixture with molecular detail.

The first issue is the hierarchy of time scales that plays a role in this phenomenon. Current understanding of the micelle–vesicle transition pathway³⁴ – formation of disc-like micelles from spherical and worm-like micelles, growth of discs to a critical size and closure into vesicles – shows that liposome formation is many orders of magnitude slower than (local) molecular reorganization, which is the essential time scale for any molecular computational model. The slowest and rate limiting step along this pathway is the growth of disc-like micelles, which has been identified to take seconds up to minutes in experimental systems. We can estimate a physical time increment based on the experimental diffusion constant of bulk water, $D = 2.3 \times 10^{-9} \text{ m}^2 \text{ s}^{-1}$ (ref. 35) and the requirement of stable time integration, *i.e.* $\Delta\tau = D\Delta t/r_c^2 \leq 0.5$, as $\Delta t \sim 10^{-9}$ to 10^{-10} s (using $r_c = 1 \text{ nm}$). Although a nanosecond is $\mathcal{O}(10^6)$ larger than the standard femtosecond time increment in molecular dynamics, it is clear that simulating the complete pathway of vesicle formation still represents a serious computational burden.

In addition, the last step, *i.e.* closing up into vesicles, gives rise to lower bounds for the size of the simulation volume. In an earlier DDFT study,³⁰ we have shown that the formation of closed membranes or vesicles from a homogeneous mixture can be prevented by (artificial) stress contributions that originate from the periodic boundary conditions. In particular, closing up is dictated by the competition between the (growing) size of the rim and the bending rigidity, meaning that discs first have to

reach a certain size before closing up. When the simulation volume is smaller or comparable to this characteristic size, discs may be stabilized and closing up is prevented. Since this characteristic size will vary with the chosen molecular model or, equivalent, the intrinsic membrane properties, we turn to experiments for guidance.

Spontaneously formed liposomes, produced by this experimental pathway,³⁴ have a typical diameter R of a few tens of nm. Considering a vesicle with radius $R/r_c = R^* = 40$, we conclude that a $L \times L \times L$ simulation volume is required, with $L > 2R^*$, to sufficiently reduce stresses due to boundary conditions. For $L = 100$, this volume contains $N_l \approx 8\pi 40^2 \times 0.79 = 3.2 \times 10^4$ lipids. In comparison with full particle (DPD) simulation, we note that the hybrid description requires only roughly 10% of the total number of particles $N = 3 \times 10^6$ for DPD.

Structure formation from the mixed state. We start with systems that are initially mixed and consider two lipid concentrations. For the lowest one, $N_l = 13\,825$ lipids were placed in a 100^3 simulation volume ($N = 3 \times 10^6$). For the highest one, a reduced volume of 50^3 , containing $N_l = 7900$ lipids, was considered ($N = 3.75 \times 10^5$). In both cases, the solvent field was initialized as $\rho(\mathbf{r}) = \bar{\rho} = N_w/N$, with $N_w = N - 11N_l$. For the considered cases, $\bar{\rho} = 0.95$ or 0.77 , respectively.

Prior to starting the simulations, a short BD simulation of the lipids, for a non-interacting stationary solvent field, was performed to disperse the lipids from their original random positions, followed by a short DDFT simulation of the solvent, for stationary lipids, to generate field exclusion profiles around lipids. The details of this equilibration are not important for the results. Consequently, hybrid simulations with $\Delta\tau = 0.04$ were performed, using default values for the diffusion coefficients and $f_{\text{up}} = 5$.

The result for the lowest concentration after 7.765×10^6 steps ($\tau = 310\,600$) is shown in Fig. 5. We find only small aggregates, reminiscent of the early stage (\leq second experimentally) of lipid self-assembly into disc-like micelles. As mentioned earlier, the growth of these micelles by lipid uptake and/or micelle coalescence is a very slow process in reality, and we expect that our simulation does not reach this stage. Moreover, our kinetic model is diffusive, and aggregates thus have to diffuse over a distance to eventually meet and merge with other aggregates. In reality, hydrodynamic interactions will accelerate this process significantly. However, even with hydrodynamics at work, the average distance between the initial aggregates increases with decreasing concentration, explaining why liposome formation is generally a slow process. It should be noted that DPD does not necessarily provide a better or more realistic account of the experimental pathway. Measured diffusion coefficients for both water and lipids were found to be substantially larger in DPD compared to experiments, and as a consequence, the structure formation dynamics is substantially accelerated.³⁵ It was also noted that ‘the diffusion between lipids in the gel phase and the liquid phase [of the membrane] differ by far less than the orders of magnitude observed experimentally’,³⁵ making attempts to set time scales in DPD by dynamics matching rather fruitless.

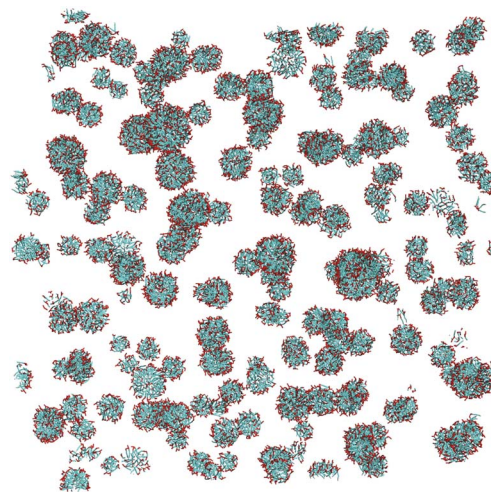


Fig. 5 Lipid self-organization into aggregates after 7.765×10^6 time steps in a 100^3 simulation volume with the hybrid method, for the lowest considered lipid fraction (~ 5 v%). The initial system is a homogeneous mixture of lipids and water. The size of the aggregates varies, but is clearly upper bounded. Blue: tail (C) particles and red: head (H) particles.

As a technical comment, we note the artificially high lipid transport rate across the membrane for our parameter set.³³ Local molecular rearrangements like these may affect the subtle balance responsible for the closing up of disc-like micelles, leading to destabilization before they reach the threshold size. We are not bothered, however, as this phenomenon can be resolved by selecting a better DPD representation. Overall, we conclude that the scale problem dictates additional measures, for instance the introduction of implicit solvent, for simulating spontaneous vesicle formation with molecular resolution.

For the higher concentration, the result after 9×10^5 steps ($\tau = 36\,000$) is shown in Fig. 6. Lipids initially assemble into small membrane patches that connect into a percolating bicontinuous network spanning the simulation volume. With time, the structure coarsens and the size of the membrane patches with a well-defined curvature increases. Defected membrane structures like this are also obtained as intermediate structures in CGMD calculations, where vesicles are assembled by starting with more concentrated systems, in a smaller volume, and subsequently diluting the lipids by increasing the volume and adding water molecules.³⁶ Compared to the less concentrated system considered before, diffusion limitations play a lesser role, as the proximity of the lipids in the initial distribution enables the formation of membrane patches from the start, and direct closing up, into small vesicles, is prevented by connections. Stabilization by the bicontinuous network is also the reason why the structure coarsening does not proceed. Although a network was already observed at early stages, we did not consider the kinetics in detail. The formation of a bicontinuous structure typically takes 20 ns in CGMD, and the transformation into a vesicle ~ 200 ns. It is known, however, that these values depend on size and initial structure.³⁶

Structure healing. As a last example, we consider healing for a pre-assembled vesicle with a hole (see Fig. 7). The

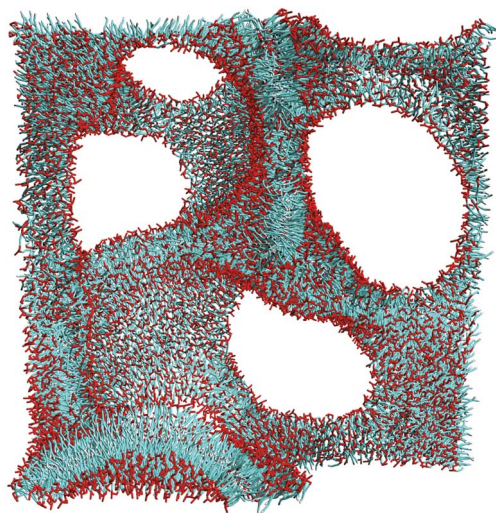


Fig. 6 A bicontinuous network of lipid bilayer patches formed after 9×10^5 time steps in a 50^3 simulation volume with the hybrid method, for the highest considered lipid fraction (~ 23 v%). The initial system is a homogeneous mixture of lipids and water. The transformation into one or more closed membranes or vesicles is prevented by the periodic boundary conditions that stabilize the connection between membrane patches. Blue: tail (C) particles and red: head (H) particles.

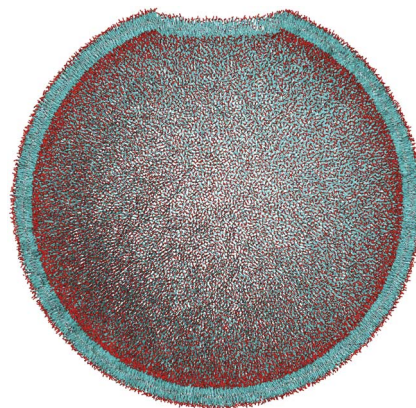


Fig. 7 Starting structure for the punctured vesicle simulation, generated following the procedure: homogeneous filling of two spherical leaflets around the midplane at $R = 45$, removal of lipids that are part of the intersection with a short cylinder centered around one of the poles and equilibration following the standard procedure. Lipids in the front part of the structure are removed for clarity. The simulation volume is 100^3 and the lipids in each of the leaflets are initially positioned in opposing directions, according to the curvature corrected thickness and fixed lipid per area fraction $lpa = 0.79$, the value for a tensionless flat membrane. Averaged values of the external and internal radii are estimated from the position of the head particles as $R_{\max} = 47.3$ and $R_{\min} = 42.7$. Blue: tail (C) particles, grey: tail terminus (E) particles and red: head (H) particles.

thermodynamic driving force for structural changes stems from the unfavorable contact between water and the hydrophobic lipid tails at the rim. Lipids can respond by either reorienting or reorganizing locally, to bury the tails inside the membrane, or by reorganizing on a larger scale to minimize the size of the rim. Pore stabilization was earlier considered,³⁷ and showed that rim stabilization is possible for giant unilamellar vesicles composed of a lipid mixture that includes lipids associated with a high spontaneous curvature. Here, only one type of lipids is present and the very large curvatures along the rim associated with the first mechanism will be avoided. The lipids will tend to reorganize collectively, to decrease the size of the rim and eventually close up.

We considered a 100^3 simulation volume ($N = 3 \times 10^6$) and pre-assembled a vesicle of radius $R = 45$ for the midplane (~ 45 nm) using the procedure described earlier. The number of lipids in the inner and outer leaflet for $lpa = 0.79$ is 17 931 and 22 398, respectively, giving rise to a total number of lipids $N_l = 40 329$. After preparation, all lipids within a cylindrical region centered around one of the poles of the membrane are removed, creating the hole (see Fig. 7). This reduces the total number of lipids to $N_l = 39 157$, or 17 380 in the inner and 21 777 in the outer leaflets, respectively. Further equilibration is performed following the guidelines presented earlier. We realize that the simulation volume is rather small for a vesicle of this size, but conclude that it is sufficient for our purpose. In particular, the solvent field swiftly levels off to a constant value for these high coupling parameters.

After equilibration, hybrid simulations were performed for 1.5×10^6 steps, with $\Delta\tau = 0.04$, using default values for the diffusion coefficients and $f_{\text{up}} = 5$. The final structure, a closed vesicle, is displayed in Fig. 8. We conclude that the anticipated

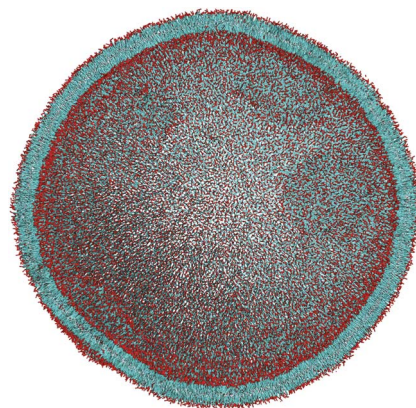


Fig. 8 Structure obtained after 1.5×10^6 time steps with the hybrid model, showing that lipid rearrangement towards vesicle closure is indeed the mechanism for minimizing the undesired curvature of the rim. Lipids in the front part of the structure are removed for clarity. The averaged values for the external and internal radii $R_{\max} = 44.2$ and $R_{\min} = 39.3$, estimated from the position of the head particles, show that the vesicle has contracted as a whole, a process that is accompanied by redistribution of lipids from the outer leaflet to the inner leaflet (523 lipids in total). Blue: tail (C) particles, grey: tail terminus (E) particles and red: head (H) particles.

mechanism, *i.e.* vesicle healing by lipid reordering on a large scale, is indeed confirmed by simulations. The number of lipids in the inner and outer leaflets at the final stage was determined as 17 903 and 21 254, indicating that the liposome has contracted as a whole *via* the redistribution of excess lipids from the outer to the inner leaflet (523 lipids). Contraction is also observed in the averaged external (internal) vesicle radius, determined from the locations of the head particles, which

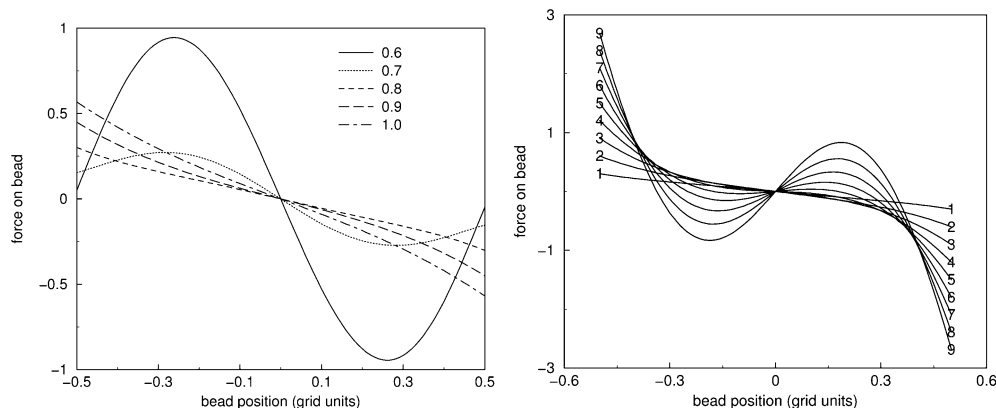


Fig. 9 Coupling force calculated using the analytic equilibrium profile and the 27-points stencil (three grid nodes) in 1D, for one particle in a monomeric field. Left: for varying σ and coupling parameter $c = 1$; right: for $\sigma = 0.8$ and varying coupling parameter $c = 1, \dots, 9$. The particle position is varied with respect to the central node located at the origin. Other parameters used were $\kappa = 4.6$ and $\rho_f^p = 3$.

reduces from $R_{\max} = 47.3$ ($R_{\min} = 42.7$) to $R_{\max} = 44.2$ ($R_{\min} = 39.3$) over time.

Visual inspection, see Fig. 8, suggests that the distribution of lipids in the leaflets is rather homogeneous. However, the vesicle also seems less spherical and a small bulge (lower left corner) is formed, suggesting composition fluctuations. Analysis of the local lipid content in the leaflets indeed shows variations and confirms that the cooperative redistribution of lipids within each of the leaflets after closure is slow. The bulge eventually develops into a small double-bilayer patch at later times.

A similar effect was observed in large closed pre-assembled vesicles that were constructed to be deformed or under stress, *i.e.* starting from an ellipsoid or with an excess amount of lipids in both bilayers (results not shown). In both cases, the results showed that local lipid rearrangements resulted in the

formation of multiple-layer patches in the original bilayer, on the pathway towards multi-lamellar vesicles. This finding raises the more general issue that, although one may assemble the membrane according to the lipid per area fraction $\text{lpa} = 0.79$ for a tensionless state taken from DPD for small, flat membranes,¹¹ there is no guarantee that the vesicle will be tensionless. We identify several possible causes for this layering. First, the restructuring pathway is limited by diffusion and the low permeability of the membrane to solvent. The latter is important to realize, as the vesicle cannot change its enclosed volume without creating a pressure difference between the inner and outer solvent in our canonical ensemble. Due to these frustrations, the system may be pushed into a different pathway. Although these factors play a role, we believe that the main cause can be found in the original parameter set of Shillcock and Lipowsky¹¹ that we use. Besides the discussed artificially high probability of lipid heads crossing through the membrane core, it is easy to see that $a_{\text{HH}} < a_{\text{HW}}$ and $a_{\text{HC}} < a_{\text{WC}}$ introduces a considerable tendency for membranes to adhere, since replacing the water adjacent to the membrane by another membrane has the effect of lowering the interaction energy.³³ The multi-layer membrane patches can be seen as locally adhering membranes, and their actual formation as a consequence of an interplay of the discussed factors. We conclude that this requires a much more careful analysis, in particular of the DPD parameterization, and we leave this for future work.

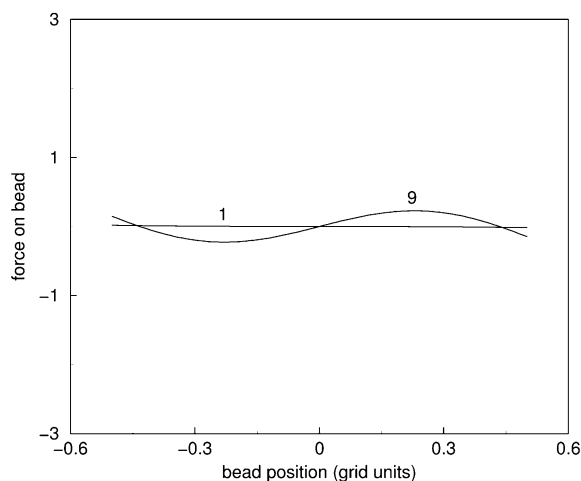


Fig. 10 Coupling force calculated for $\sigma = 1.0$ and varying coupling parameter $c = 1$ and 9, using the analytic equilibrium profile and the 125-points stencil (five grid nodes) in 1D, for one particle in a monomeric field. The particle position is varied with respect to the central node located at the origin. Other parameters used were $\kappa = 4.6$ and $\rho_f^p = 3$.

Conclusions

We have developed a versatile model that binds together two popular mesoscopic descriptions. Soft-core particles from DPD can be used to represent the sparse constituents or constituents for which explicit chain conformations are important. Fields from molecular field theory can represent the abundant constituents, or the constituents for which a mean field description suffices. This freedom of representation not only allows for adding molecular detail to field-based simulations, but also for an increased efficiency of particle-based simulations. Particles and fields are made to interact with each other

via a new coupling term that accounts for both the excluded volume and the cohesive interactions. Thermodynamic consistency was used to derive expressions or mappings that directly relate new coupling parameters to mean-field χ and/or DPD a parameters. The validity of this map was numerically tested *via* solubility calculations.

Our starting point for validation is a coarse-grained model for DMPC lipids in water. We use parameters that are mapped from an existing DPD model by Shillcock and Lipowsky. We find a stable pre-formed membrane with a profile that agrees very well with the result of DPD simulations. Analysis of the surface tension in the new approach was found to be more complicated, and we decided to postpone such a study. In addition, we considered proof-of-principle simulations for a few large-scale target systems. For low lipid concentrations, simulations are incapable of reaching the later stages of vesicle formation from a homogeneous mixture. The standard solution, *i.e.* starting with an increased lipid concentration and diluting afterwards, indeed resolves this issue and gives rise to the formation of a bicontinuous network. It shows that the increased efficiency, at the expense of diffusion limitation, does not resolve the general issues of molecular modeling. Nevertheless, the introduction of implicit solvent would further reduce the computational requirements and bring these slow, collective processes within reach, and the current method can serve as a first step for the analytical introduction of implicit solvent in DPD. Simulating from a pre-assembled structure, a punctured vesicle, shows the anticipated mechanism: the size of the rim that surround the hole decreases and the hole finally closes up, diminishing the energy costs associated with high rim curvature. We find that lipid reorganization in regions of excess lipid concentration in a closed vesicle results in the formation of patches bearing multiple layers. Several factors may cause this unexpected result, including the chosen DPD parameter set, which was previously shown to give rise to anomalous lipid flip-flop rates. The efficiency of the new method, and the additional efficiency gained after the introduction of implicit solvent, (will) enable(s) elaborate parameter/property scans on the scale of complete vesicles.

Next, this model will serve as a starting point for the introduction of implicit solvent into DPD. Since all processes are diffusion-limited in the current model, a possible extension is to couple particle DPD to a Lattice-Boltzmann model for the field.³⁸ Such extensions will be considered in the near future.

Appendix A: numerical considerations

In the numerical implementation of the hybrid system, particles and field are treated on a different footing. Although the chain conformations underlying the molecular field are not spatially restricted, concentration fields are calculated and evolved using a (cubic) lattice. Field values are stored in the center of each computational cell. The particle representation is essentially mesh-free, but the field mesh is used for efficient calculation of particle–particle interactions in practice, in a staggered fashion. The Gaussian smoothing kernel facilitates a map from a particle coordinate to a field. The spread σ in the Gaussian kernel determines the *range* of the interactions, and

can be used to tune local properties, in particular at the interface between particles and fields. One should, however, be careful not to introduce interpolation or long range interactions in the hybrid model as they will hamper the computational efficiency. Special care is given to the discrete procedures (stencils) for integration and differentiation.

We rely on the discrete representations for the Laplacian and Gaussian convolutions (quadrature rules) for field-based DDFT.^{16,39} In both cases, these operators were derived based on efficiency and accuracy, *i.e.* proper stencil weights for the most compact 27-points stencil – the grid node itself and all nearest-neighbors in 3-D – were determined based on conserving the isotropy and scaling properties of the continuum operators. The regularity of the grid as well as the symmetry of the Gaussian kernel around grid positions was explicitly exploited in the derivation of stencil weights and vital for the accuracy. Applying the same stencils for the coupling kernel, which is centered around an arbitrary off-grid position \mathbf{r}_p , may thus have the undesired effect of introducing anisotropy or grid artifacts into the simulation.

Instead of using these quadrature rules for a particle-centered stencil, which would require interpolation of field values for off-grid locations, we approximated the integral by the normalized truncated Riemann sum. It is clear that both the spread σ and the size of the computational stencil are important for the error made in this approximation. We again considered a compact stencil, the 27 grid-points closest to the particle coordinate, and numerically analyzed this error, by considering the coupling force for a single particle that is pulled (by a constant force) through a field, where the pulling is slow enough to allow for field equilibration. We found that the amplitude of the fluctuations of the coupling force are smallest for $\sigma = 0.8$. Analytical calculations (see next section) of the coupling force on a single particle, as a function of the off-grid particle coordinate in 1-D, corroborate the numerical finding of an optimal $\sigma = 0.8$, see Fig. 9 (left). In Fig. 9 (right), the coupling force for increasing coupling strengths is plotted against the particle position and a vanishing force for three distinct particle positions can be identified, two of which depend on the coupling parameter. One may observe the discontinuity in the force that is encountered when the particle crosses over to a position associated with a stencil centered around another central node. However, we conclude that this bias is rather insignificant, since the conservative forces due to particle–particle interactions will dominate the behavior in domains with high particle concentrations. This conclusion is further justified by the fact that we did not observe distinct field–grid related phenomena in our simulations. For cases where this artificial force is important, however, extending the stencil to 125 grid points is a viable option. Fig. 10 shows a significantly decreased artificial force for $\sigma = 1$, at the expense of slightly reduced computational efficiency.

Appendix B: the volume for a single particle in a field

Most analytic results in this paper were derived assuming a significantly high particle density, $\rho_p > 2$. In many realistic

cases, particles describe a minority component and $\rho_p < 2$. Nevertheless, since the particles and the field are often immiscible, particle clusters with relatively high internal density will form and the assumption is again valid inside the clusters. We note that a very similar reasoning was used to rationalize mean-field treatments of semi-dilute cases. Although a mean-field treatment of specific interactions is strictly justified only for melts, in practice both methods have been successfully applied to describe structure formation in semi-dilute cases, using χ determined for melts. An attractive example is the existing mean-field treatment of amphiphilic (A_iB_j) membranes in an aqueous (S) environment, where the concentration of the amphiphile $\rho_{A+B} \leq 0.1-0.2$.³⁰

Here, we turn to the other side of the spectrum and consider a mixed system that is almost totally monomeric field, except for a single particle, and estimate the excluded volume of this particle. The particle is fixed at the origin of the coordinate system and the field subsystem is assumed to have reached equilibrium state, *i.e.* the free energy functional eqn (4) is minimal and the total chemical potential eqn (34) is homogeneous in V . In particular, the bulk chemical potential

$$\mu_f^b = \ln \rho_f^b + \kappa_H \rho_f^b \quad (37)$$

far from the particle, where the coupling contribution vanishes, balances the chemical potential at a distance r from the particle

$$\mu_f(r) = \ln \rho_f(r) + \kappa_H \rho_f(r) + cK(r) \quad (38)$$

due to the assumption of equilibrium, and we obtain

$$\ln \frac{\rho_f(r)}{\rho_f^b} + \kappa_H \rho_f(r) + cK(r) - \kappa_H \rho_f^b = 0 \quad (39)$$

Using the Lambert function W , the field density $\rho_f(r)$ follows as

$$\rho_f(r) = \frac{1}{\kappa_H} W \left(\kappa_H \rho_f^b e^{\kappa_H \rho_f^b - cK(r)} \right) \quad (40)$$

where r is the distance from the particle. Since the Lambert function W can not be further simplified in terms of more common elementary functions, this solution can be evaluated numerically, but it is not very convenient for further analysis. Using only the first term of a Taylor expansion

$$\ln(x) = \sum_{n=1}^{\infty} \frac{(-1)^{n+1}}{n} (x-1)^n \quad (41)$$

instead, it can be shown that the density profile eqn (40) can be approximated, for low c values or $\rho_f(r) \approx \rho_f^b$, considerably well by

$$\rho_f(r) \approx \rho_f^b \left(1 - \frac{cK(r)}{1 + \kappa_H \rho_f^b} \right). \quad (42)$$

This limited validity of this expression is reflected by the fact that $\rho_f(r)$ cannot become negative. The relation eqn (42) shows that the density profile of the monomeric field for small c has an inverted Gaussian shape, with the minimum field value in the center of the particle. We define the effective volume of the particle as

$$v_p = \frac{1}{\rho_f^b} \int_V d\mathbf{r} (\rho_f^b - \rho(r)) \approx \int_V d\mathbf{r} \frac{cK(r)}{1 + \kappa_H \rho_f^b} = \frac{c}{1 + \kappa_H \rho_f^b} \quad (43)$$

and find that it scales linearly with c . The corresponding coupling energy is

$$\begin{aligned} F_{\text{coup}}^1 &= c \int d\mathbf{r} K(r) \rho_f(r) \approx c \rho_f^b - \frac{c^2 \rho_f^b}{1 + \kappa_H \rho_f^b} \int d\mathbf{r} K^2(r) \\ &\approx c \rho_f^b \left(1 - \frac{0.124c}{1 + \kappa_H \rho_f^b} \right). \end{aligned} \quad (44)$$

Acknowledgements

We thank Karol Langner for his contributions during the development and simulation stage and Andrei Zvelindovsky and Friederike Schmid for stimulating discussions. This work was funded by the VW foundation.

References

- 1 J. C. Faver, M. L. Benson, X. He, B. P. Roberts, B. Wand, M. S. Marshall, C. D. Sherill and K. M. Merz Jr, *PLoS One*, 2011, **6**, e18868.
- 2 M. Venturoli, M. Maddalena Sperotto, M. Kranenburg and B. Smit, *Phys. Rep.*, 2006, **437**, 1.
- 3 M. Müller, K. Katsov and M. Schick, *Phys. Rep.*, 2006, **434**, 113.
- 4 M. Deserno, *Macromol. Rapid Commun.*, 2009, **30**, 752.
- 5 S. J. Marrink and A. E. Mark, *J. Am. Chem. Soc.*, 2003, **125**, 15233.
- 6 L. Saiz, S. Bandyopadhyay and M. L. Klein, *Biosci. Rep.*, 2002, **22**, 151.
- 7 G. S. Ayton and G. A. Voth, *J. Phys. Chem. B*, 2009, **113**, 4413.
- 8 M. Maddalena Sperotto, S. May and A. Baumgaertner, *Chem. Phys. Lipids*, 2006, **141**, 2.
- 9 G. Gulgas, D. Morozova and M. Weiss, *Adv. Protein Chem. Struct. Biol.*, 2011, **85**, 143.
- 10 M. Kranenburg, J. P. Nicolas and B. Smit, *Phys. Chem. Chem. Phys.*, 2004, **6**, 4142.
- 11 J. C. Shillcock and R. Lipowsky, *J. Chem. Phys.*, 2002, **117**, 5048.
- 12 Z.-J. Zhang and M. Deserno, *New J. Phys.*, 2010, **12**, 095004.
- 13 H. A. Karimi-Varzaneh and F. Müller-Plathe, in *Multiscale Molecular Methods in Applied Chemistry*, ed. A. E. Algaer and F. Müller-Plathe, 2012, vol. 307, p. 295.
- 14 K. Ch. Daoulas and M. Müller, *J. Chem. Phys.*, 2006, **125**, 184904.
- 15 A. De Nicola, Y. Zhao, T. Kawakatsu, D. Roccatano and G. Milano, *J. Chem. Theory Comput.*, 2011, **7**, 2947.
- 16 B. A. C. van Vlimmeren, N. M. Maurits, A. V. Zvelindovsky, G. J. A. Sevink and J. G. E. M. Fraaije, *Macromolecules*, 1999, **32**, 646.
- 17 R. D. Groot and P. B. Warren, *J. Chem. Phys.*, 1997, **107**, 4423.
- 18 E. Helfand, *J. Chem. Phys.*, 1975, **62**, 999.

- 19 H. D. Cenicerros and G. H. Fredrickson, *Multiscale Model. Simul.*, 2004, **2**, 452.
- 20 T. Kawakatsu, *Statistical Physics of Polymers: An Introduction*, Springer, 2004.
- 21 I. Pagonabarraga, M. H. J. Hagen and D. Frenkel, *Europhys. Lett.*, 1998, **42**, 377.
- 22 L. Gao, J. Shillcock and R. Lipowsky, *J. Chem. Phys.*, 2007, **126**, 015101.
- 23 N. M. Maurits, A. V. Zvelindovsky and J. G. E. M. Fraaije, *J. Chem. Phys.*, 1998, **108**, 2638.
- 24 R. M. Fuchslin, H. Fellermann, A. Eriksson and H. J. Ziock, *J. Chem. Phys.*, 2009, **130**, 214102.
- 25 S. H. L. Klapp, D. J. Diestler and M. Schoen, *J. Phys.: Condens. Matter*, 2004, **16**, 7331.
- 26 R. D. Groot and T. J. Madden, *J. Chem. Phys.*, 1998, **108**, 8713.
- 27 C. W. Gardiner, *Handbook of Stochastic Methods*, Springer, Berlin, 2004.
- 28 A. Knoll, K. S. Lyakhova, A. Horvat, G. Krausch, G. J. A. Sevink, A. V. Zvelindovsky and R. Magerle, *Nat. Mater.*, 2004, **3**, 886.
- 29 X. H. He and F. Schmid, *Macromolecules*, 2006, **39**, 2654.
- 30 G. J. A. Sevink and A. V. Zvelindovsky, *Macromolecules*, 2005, **38**, 7502.
- 31 T. Uneyama and M. Doi, *Macromolecules*, 2007, **126**, 114902.
- 32 N. M. Maurits and J. G. E. M. Fraaije, *J. Chem. Phys.*, 1997, **107**, 5879.
- 33 A. Graftmüller, J. Shillcock and R. Lipowsky, *Biophys. J.*, 2009, **96**, 2658.
- 34 J. Leng, S. U. Egelhaaf and M. E. Cates, *Europhys. Lett.*, 2002, **59**, 311; J. Leng, S. U. Egelhaaf and M. E. Cates, *Biophys. J.*, 2003, **85**, 1624.
- 35 J. M. Rodgers, J. Sørensen, F. J.-M. de Meyer, B. Schiøtt and B. Smit, *J. Phys. Chem. B*, 2012, **116**, 1551.
- 36 W. Shinoda, R. DeVane and M. Klein, *Curr. Opin. Struct. Biol.*, 2012, **22**, 175.
- 37 Y. Sakuma, T. Taniguchi and M. Imai, *Biophys. J.*, 2010, **99**, 472.
- 38 L. Zhang, G. J. A. Sevink and F. Schmid, *Macromolecules*, 2011, **44**, 9434.
- 39 N. M. Maurits, J. G. E. M. Fraaije, P. Altevogt and O. A. Evers, *Comput. Theor. Polym. Sci.*, 1996, **6**, 1.